Rev. Roum. Sci. Techn.– Électrotechn. et Énerg.
Vol. **67**, *4*, pp. 417–423, Bucarest, 2022

IMPROVED ACTIVE TORQUE PULSATION REDUCTION METHOD FOR PULSATING LOADS DRIVEN BY INDUCTION MACHINES

ADRIAN DANIEL MARTIN [1], LUCIAN TUTELEA [2], RADU BABAU [3], ION BOLDEA [4]

Keywords: Active torque control; Induction machine; Luenberger-based observer; Mechanical parameters-free control.

An online active torque pulsation reduction strategy for rotational systems with position-dependent loading torque (such as crankshaft-based loads) driven by grid-connected induction machines is proposed. The control strategy requires system speed and induction machine torque information. No stiff parameters are necessary for the closed-loop control strategy. The theoretical principle is simulated and experimentally validated.

1. INTRODUCTION

The active torque pulsation reduction method (ATPRM) technique is commonly used in many industries, from micro to macro applications (in construction, robots, automotive, hearing, oil and gas, CNC, aeronautics, *etc*.). It is a particular application of the well-known so-called active vibration control (AVC) techniques.

AVC involves an external force added into the system of the opposite phase and the same amplitude (or smaller) as the force created by the disturbance (main vibration force). Several techniques are stated in [1], [2].

For many years, the AVC has been used to minimize the negative impact of vibration over a mechanical structure by total vibration reduction (vibration-free systems) or partial vibration reduction.

Such modern active vibration applications are spread worldwide and used in constructions [3] or automotive [4], [5], where the suppression of pulsations/vibrations is realized both for safety and comfort. In recent years, the use of functionally graded piezoelectric material (FGPM) as an actuator for active vibration control has been crucial in the aeronautics [6]. Besides that, conventional active masses ([7]) can be used as a counterbalance in vibration-producing systems.

Based on the same principle (AVC), recently, active noise cancellation (ANC) received more interest from the industries. One can find such applications in most headphones [8]–[10]. The authors propose a new technique for engine noise cancelation based on active noise control.

In linear mechanical systems, the superimposed (added) active force is represented by a linear force; on the other hand, in rotary electromechanical systems, the perturbance force is represented by the torque. This way, the superimposed (compensation) active force is characterized by a 180 deg phase-shifted torque.

A distinct type of pulsating loading torque is produced in electromechanical systems with position-dependent load torque variations. Such position-varying load torque is found in piston-based loads (*e.g.*, reciprocating compressors). Compared to applications where the load torque varies relatively slowly (pump, fan, conveyor belts, etc.), the position-dependent load torque imposes a higher response frequency than in a standard AVC technique.

For inverter-fed electrical machine-driven applications, such ATPRM can be achieved by directly controlling the variable frequency inverter. Several such methods are proposed in [11], [12]. Passive solutions for smoothing the pulsating torque are reported in [13], where crankshaft torsional absorbers or shaft flywheels are used.

This paper simulates and experimentally validates the principle of the active torque pulsation reduction method (ATPRM) of position variable loads driven by a grid-connected induction machine (GCIM) with an additional on-shaft auxiliary smaller machine (AM).

Figure 1 presents the basic principle used in this paper: a new auxiliary machine (AM), driven by a variable frequency converter (VFC), is added to the existing on-site electromechanical system to suppress the second and third torque harmonics of the pulsating load torque (*e.g.*, reciprocating compressors), thus smoothing it to a significant degree.

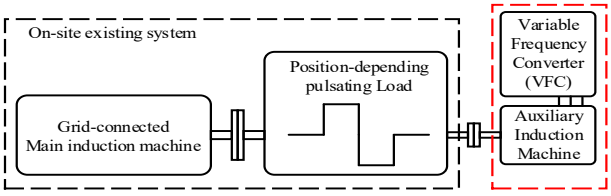

Fig. 1 – Principle schematic diagram

Figure 2 shows the general experimental setup diagram. The pulsating load is emulated by a 30 kW induction machine driven by a 25 kVA variable frequency converter.

The electromagnetic torque of the grid-connected induction machine (GCIM) is estimated online from the acquired U, I, and used in the closed-loop control strategy (section 4 – simulation). The programmable logical controller (PLC) references the position-dependent variable load torque (thus emulating a reciprocating compressor torque profile) and applies (to AM-VFC) the compensating torque reference. The GCIM torque and currents frequency spectrum is also presented and investigated. The literature [14], [15] shows that such highly pulsating load torques can be decomposed into a continuous component (dc offset) equal to 70 % of the GCIM's rated torque, overlapped by higher torque harmonics up to 30 % of the rated torque. Thus, the AM can be smaller than GCIM (20 %-30 % of its power).

The principal claimed contribution of the present paper is implementing a practical Luenberger IM torque estimation, an auxiliary inverter-fed IM method to reduce pulsating torque of main IM via an open loop control with simulation, and experimental validation of a close-loop method with simulations.

[1] University Politehnica of Timisoara, Timisoara, Romania, E-mail: adrian.martin@upt.ro
[2] Romanian Academy, Timisoara Branch, Timisoara, Romania: E-mail: ion.boldea@upt.ro
[3] S.C. Beespeed Automatizari SRL, Timisoara, Romania, E-mail: rbabau@beespeed.ro
[4] Romanian Academy, Timisoara Branch, Timisoara, Romania: E-mail: lucian.tutelea@upt.ro

The paper is structured as follows: section 2 outlines the simulation of the proposed principle of operation in line with the actual experimental setup, section 3 presents the experimental validating results, and section 4 simulates a control technique for active torque pulsation compensation in rotary mechanical systems, using the grid-connected and auxiliary motors estimated torques.

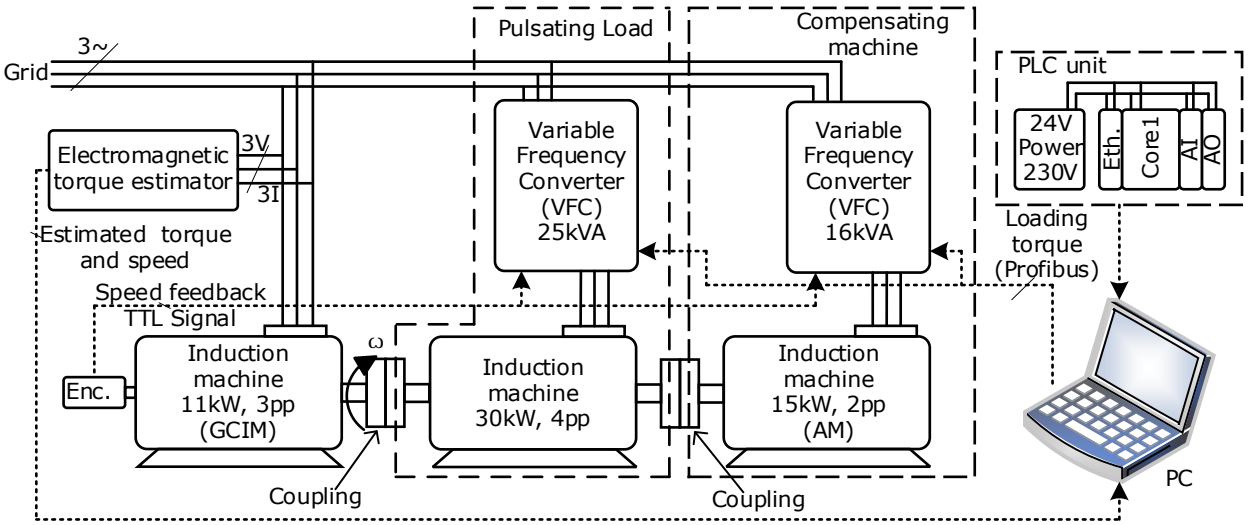

Fig. 2 – General schematic diagram.

2. OPEN-LOOP CONTROL – SIMULATION

In this chapter, both the torque and speed estimator operation and the ATPRM are studied. Figure 3 represents the simulation diagram. The red /dashed part represents the closed-loop control used and extended in section 4.

To validate the principle of operation, the "Selector" block sets the input on terminal 1, where a constant amplitude for the auxiliary motor is given. Input terminal 2 gives the closed-loop compensation amplitude for AM's drive.

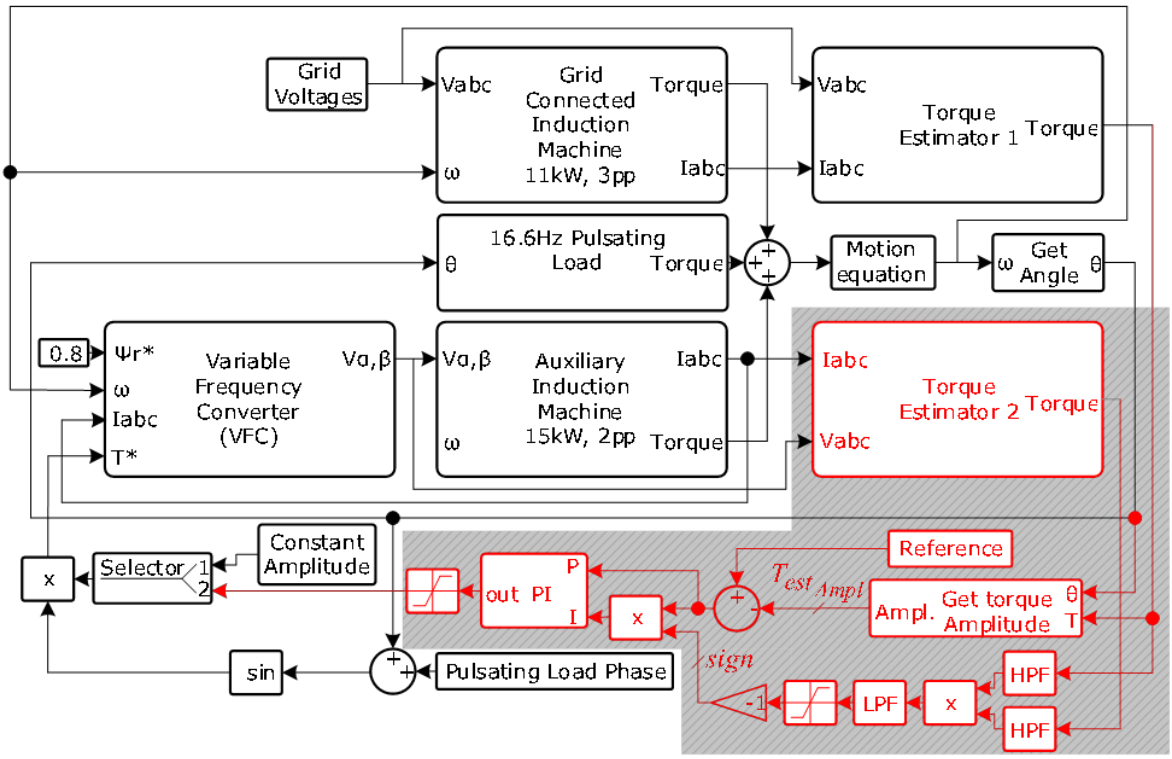

Fig. 3 – Simulation diagram for open-loop and closed-loop (red/dashed) ATPRM.

The "Pulsating Load" block produces the loading torque. The "Grid-connected Induction Machine" represents the main motor. The simulation is performed for ideal conditions, when the "Grid Voltages" block produces ideal voltages, and for "real" simulated conditions, when the supply voltages contain simulated harmonics and inverse components. Results are presented in Fig. 4, where the GCIM estimated torque is given for a 0 to rated-power step signal response. The "Torque

Estimator" block contains a Luenberger-based inherently sensorless observer, described in eqs. (1)-(9). More information about the here presented flux observer can be found in [16], [17]. Acceptable results are obtained when the speed is estimated as given in [18]. Based on the IM's dynamic model and considering the IM losses (not presented), the system speed results from the motion equation, where the estimated torque and the system moment of inertia were considered. More IM's models can also be found in [19–21].

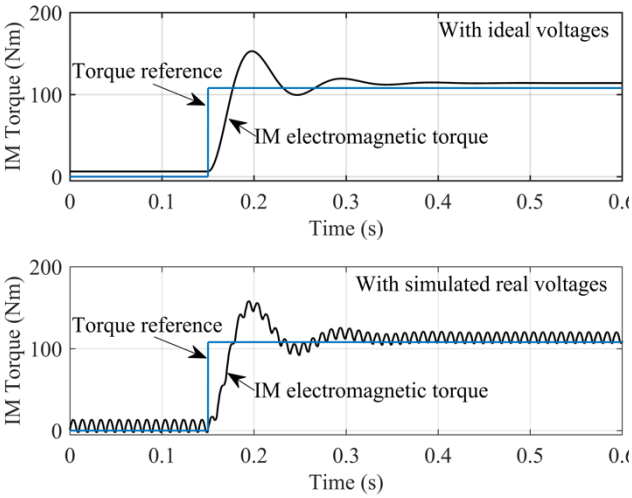

Fig. 4 – GCIM 0 to rated torque step response for a) ideal voltages and b) "real" voltages – simulation.

A variable frequency converter drives the auxiliary (additional) motor. The system speed is given in simulation by the "Motion Equation" block, which uses the total inertia of the system for speed calculations.

Considering the position-dependent pulsating load operation principle, the loading torque angle is usually known and fixed. This way, for both principle of operation (open-loop method) validation and closed-loop ATPRM, the loading angle ("pulsating Load Phase" block Fig. 3) is considered constant. It does not change significantly over time (more details in Fig. 15).

It must be stated that the mechanical coupling characteristics between the machines (such as the backlash) were not considered in the simulation.

$$\psi_{s_{\alpha/\beta}} = \int \left(v_s - i_s \cdot R_s + k_1 \cdot \left(i_s - \hat{i}_s \right) \right)_{\alpha/\beta}, \quad (1)$$

$$\hat{\psi}_{r_{\alpha/\beta}} = \psi_{s_{\alpha/\beta}} \cdot \frac{L_r}{L_m} - i_{s_{\alpha/\beta}} \cdot \frac{L_s \cdot L_r}{L_m} \cdot \sigma, \quad (2)$$

$$\sin(\theta) = \frac{\psi_{r\alpha}}{\sqrt{\psi_{r\alpha}^2 + \psi_{r\beta}^2}}, \quad (3)$$

$$\cos(\theta) = \frac{\psi_{r\beta}}{\sqrt{\psi_{r\alpha}^2 + \psi_{r\beta}^2}}, \quad (4)$$

$$\hat{i}_{s_{\alpha/\beta}} = -\hat{\psi}_{r_{\alpha/\beta}} \cdot \frac{L_m}{L_s \cdot L_r \cdot \sigma} + \hat{\psi}_{s_{\alpha/\beta}} \cdot \frac{1}{L_s \cdot \sigma}, \quad (5)$$

$$c_{\alpha/\beta} = \left(i_{s_{\alpha/\beta}} - \hat{i}_{s_{\alpha/\beta}} \right) \cdot \frac{L_s \cdot T_r \cdot \sigma}{L_m}, \quad (6)$$

$$\psi_{r(s)_{\alpha/\beta}} = I.P\left(LPF_{T_r\sigma}^{L_m/T_s} \left(P(\psi_{s_{\alpha/\beta}} + k_2 \cdot c) \right) \right) \quad (7)$$

$$T_{elm} = p \cdot \frac{3}{2} \cdot \frac{(\sigma - 1)}{(\sigma \cdot L_m)} \cdot \left(\psi_{s\alpha} \cdot \psi_{r\beta} - \psi_{s\beta} \cdot \psi_{r\alpha} \right), \quad (8)$$

$$\sigma = 1 - \frac{L_m^2}{L_s \cdot L_r}, \quad (9)$$

where: $\hat{\psi}_{s_{\alpha/\beta}}, \hat{\psi}_{r_{\alpha/\beta}}, \hat{i}_{s_{\alpha/\beta}}$, represents the estimated α,β stator, current, and rotor flux, $v_{s_{\alpha/\beta}}, i_{s_{\alpha/\beta}}, \psi_{s_{\alpha/\beta}}, \psi_{r_{\alpha/\beta}}$ are the stator α,β voltage, current and stator and rotor flux, $\psi_{r(s)_{\alpha/\beta}}$ is the α,β rotor flux in stator coordinates, R_s, L_s are stator resistance and inductance, L_r, L_m are the rotor and magnetizing inductance, k_1, k_2, σ are constants, $c_{\alpha/\beta}$ represents the α,β components of an intermediate value, $I.P, P, LPF$ represents the Park and inverse Park Transform, and a Low Pass Filter, T_s, T_r are the stator and rotor time constant, T_{elm}, p represents the estimated electromagnetic torque and number of pole pairs.

The voltage used for stator flux estimation is being corrected (besides the stator resistance voltage drop) by a factor (k1<0) applied to the error between the measured and estimated currents. The rotor flux is low pass filtered in the rotor frame. The IM parameters represent the Lowpass Filter parameters. The sin and cos values of the rotor position (angle) are needed for direct and inverse Park transform.

In Fig. 5 and Fig. 6, an automatic loading operation is performed in simulation (similar results are given from experiments in Fig. 8, 9, and 10, section 3).

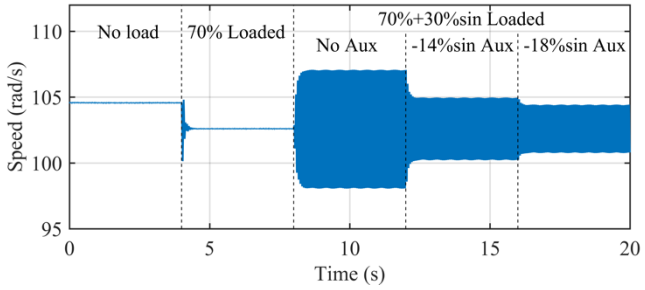

Fig. 5 – GCIM estimated speed for two compensation levels – simulation.

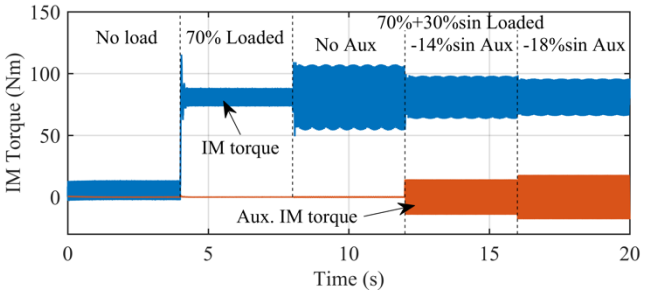

Fig. 6 – GCIM and aux. motor estimated torque – simulation.

The automatic loading process is divided into five sectors: 0-4 s where the GCIM is not loaded, 4-8 s the GCIM is loaded at 70 % rated torque dc offset (GCIM rated torque = 108 Nm), 8-12 s a 30 % of rated torque sinusoidal load is overlapped over the dc offset, 12-16 s when the AM compensates 14 % of GCIM rated torque, 16-20 s when the AM compensates 18 % of GCIM rated torque. As expected, the GCIM torque decreases in amplitude with the increase of the auxiliary IM torque. Without compensation, with a 30 % rated torque sinusoidal component, the estimated speed varies with load torque frequency by more

than 8 % of the no-load speed (Fig. 5). In this case, the GCIM power has 6 kW peak-to-peak variations. With 46 % of the pulsating torque amplitude compensation, the GCIM power amplitude drops by 25 %, while the aux. IM has a power pulsation amplitude of 39 % of the peak-to-peak GCIM power. For a 60 % pulsating torque amplitude compensation, the amplitude of the GCIM power decreases by 40 %, while the amplitude of the Aux. motor power represents 53 % of the GCIM power. For both compensation levels, the peak-to-peak amplitude of the aux. IM power is around 13 % larger than the percentage by which the GCIM power decreased.

Figure 7 shows the variation in the amplitude of the GCIM and Aux. IM power, and the sum of them, which is absorbed from the grid as a percentage of the GCIM-rated power, depending on the compensation level. It can be seen from Fig. 7 that from a grid power point of view, the amplitude of the electrical power absorbed is minimal when the torque compensation amplitude does not exceed 45% of the pulsating loading torque.

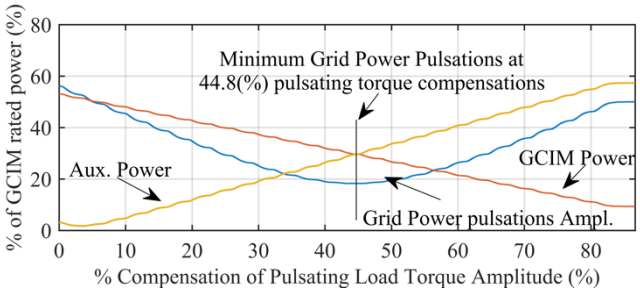

Fig. 7 – GCIM absorbed power, aux. machine absorbed power and total absorbed power variations for different compensation levels – simulation.

3. EXPERIMENTAL VALIDATION

The experiments aim to prove the theoretical principle of ATPRM in rotary electromechanical systems with an additional on-shaft reduced power machine. In Fig. 8, the experimental setup is presented.

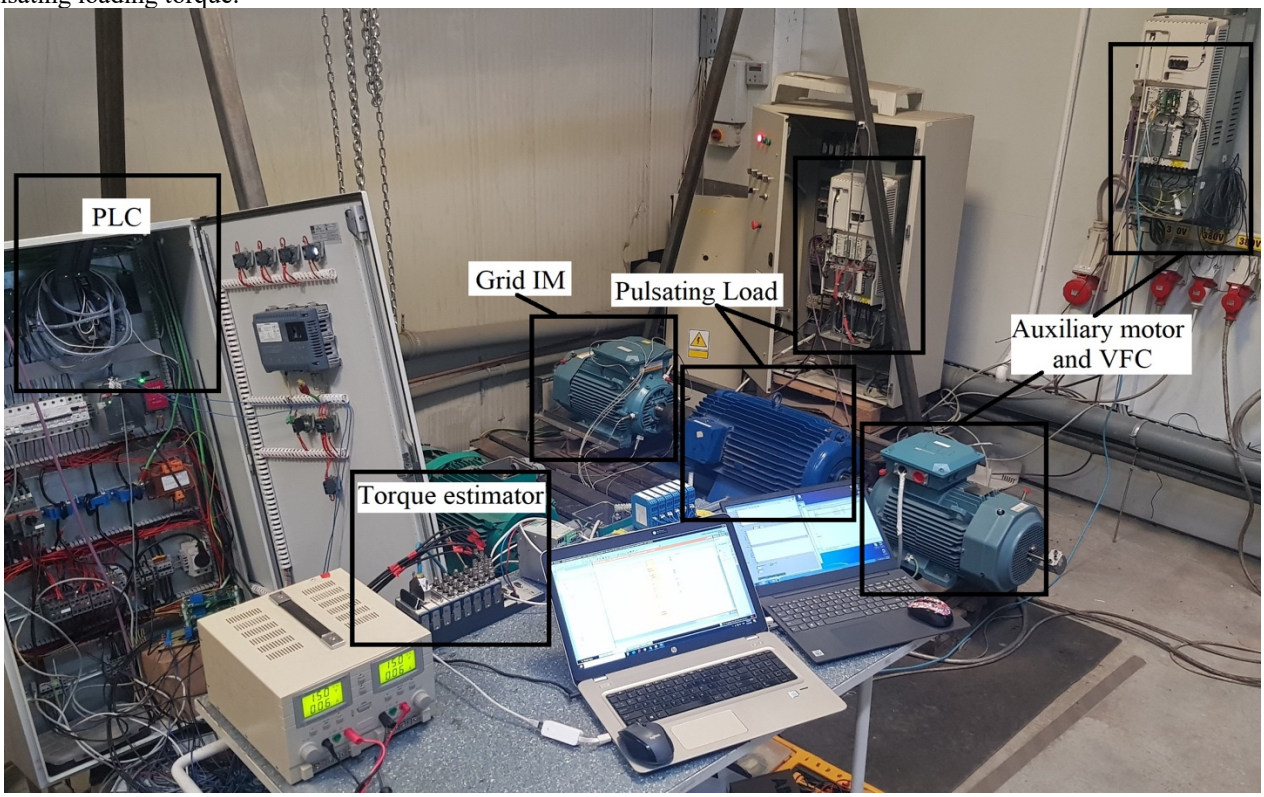

Fig. 8 – Experimental setup.

The VFC commands were given via the Profibus interface from PLC, while the torque and speed estimator were implemented into the cRio-9068 platform. The slight differences that appear compared to simulations are also due to the mechanical couplings and voltage asymmetry. Moreover, the PLC to VFCs references is unsynchronized, alternatively interlapped, at every 2ms. However, the speed pulsations are reduced as the torque compensation increases. In Fig. 9, 10, and 11, the GCIM estimated speed, torque, and the envelope of the measured currents are presented in the same conditions as in section 2 (Fig. 5 and 6).

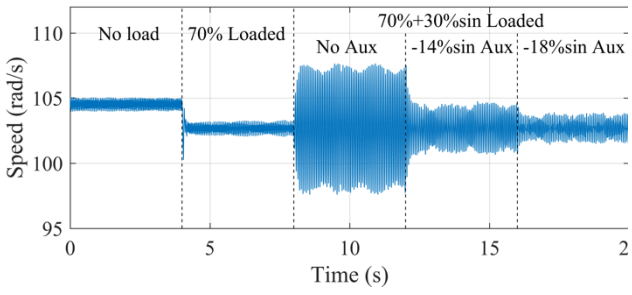

Fig. 9 – Grid connected IM's online estimated speed – measurements.

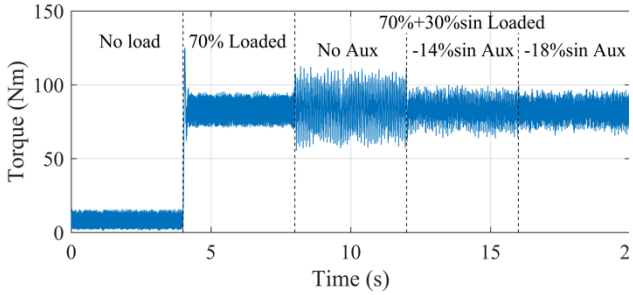

Fig. 10 – Grid connected IM's online estimated torque – measurements.

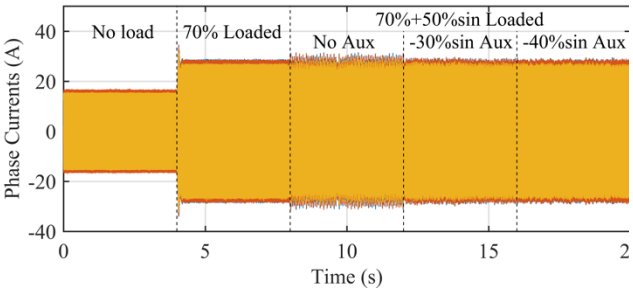

Fig. 11 – Grid connected IM's measured phase currents – measurements.

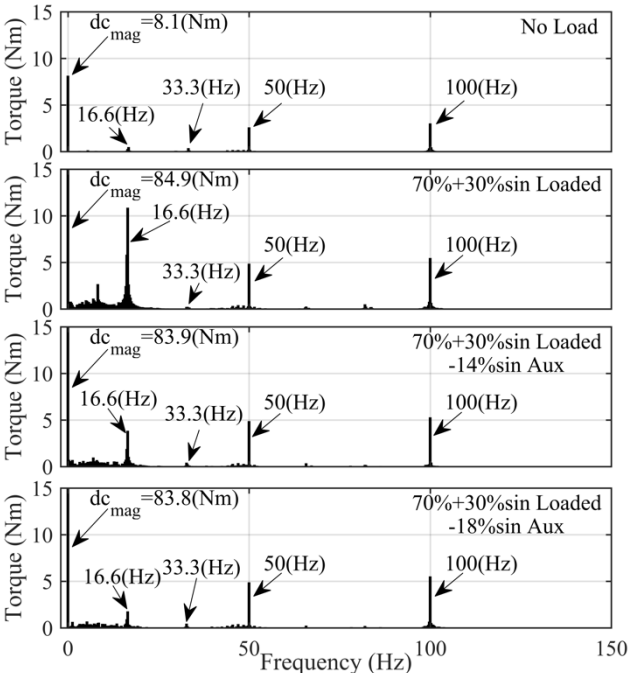

Fig. 12 – FFT on IM's online estimated torque – measurements.

Figures 12 and 13 show the Fast Fourier Transform (FFT) analysis of the frequency spectrum on the estimated torque and the measured currents for all four situations: GCIM no-load, GCIM with sine load without compensation, GCIM with load and 14 % compensation, GCIM with loading and 18 % compensation. For the no-load case, the dc component represents the IM losses; in the other cases, the load torque also appears (70 % dc component = 75.6 Nm). The 16.6 Hz component appears in the FFT when sinusoidal loading occurs. Increasing the pulsating torque compensation can be seen at 16.66 Hz frequency amplitude.

Figure 13 shows the active torque compensation effect in the 16.6 Hz apart paired harmonics eq. (10) compared to the phase current fundamental (50Hz). The reduction rate of the harmonic amplitudes is given for both compensation levels considering the no-compensation situation.

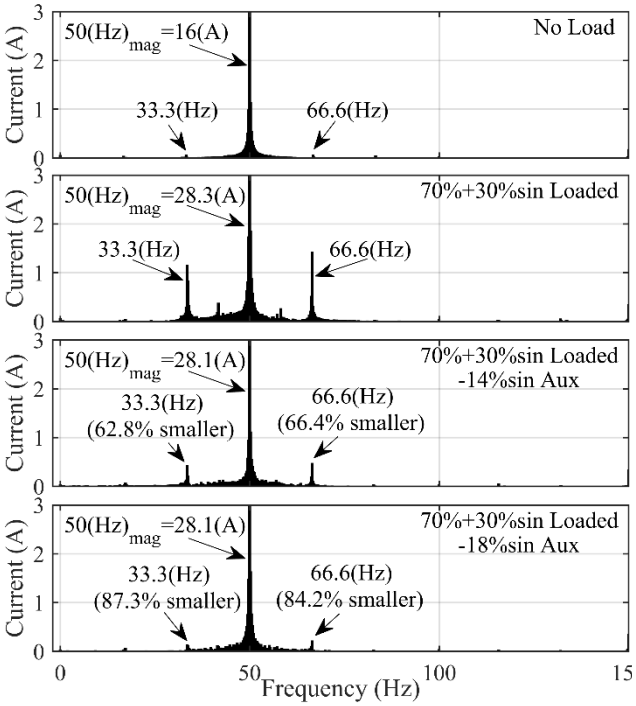

Fig. 13 – FFT on IM's measured currents – measurements.

$$\sin(a)\cdot\sin(b)=\frac{1}{2}\cdot\left(\cos(a-b)-\cos(a+b)\right), \quad (10)$$

where a and b represents the phase current frequency (50 Hz) and, respectively, pulsating loading torque first harmonic frequency (16.66 Hz)

4. PROPOSED CLOSED-LOOP CONTROL STRATEGY

Encouraged by the experimental validation of the torque pulsation reduction open-loop method, we hereby propose a closed-loop active torque control (red/dashed part Fig. 3) method that aims to minimize the amplitude of the grid-connected induction machine torque (and, consequently, current) pulsations. To do so, a different torque estimator is used to determine the auxiliary machine's electromagnetic torque, which will be further used for maintaining the right phase angle in the compensation process.

The "Get torque amplitude" block (Fig. 3) determines (according to eq. (11), (12) the GCIM electromagnetic torque pulsations amplitude, later used as a feedback loop for the PI regulator. The reference ("Reference" block) is, in essence, the maximum allowed value of the GCIM torque amplitude. Thus, the VFC drives the auxiliary machine in such a way that the torque pulsations decrease to the desired value.

High-pass filters remove the dc component from the loading torque. The Low Pass Filters are used to eliminate the torque pulsations caused by the grid voltages (those shown in detail in Fig. 4, b), which appear at multiple frequencies of the machine pole pairs.

In Fig. 14, the GCIM torque and auxiliary machine torque for closed-loop control are given. For "no compensation" regions, the loading torque produces oscillations.

To maintain the correct phase shift (180 deg) between the compensation and load torque, a sign correction is used in the integrator component of the PI controller (eq. (13).

$$\left.\begin{aligned}\sin\limits_{\wedge}{}_{T} &= Mean\left(\hat{T}_{GCIM}\right)\cdot\int\left(\hat{T}\cdot\sin\theta\right)dt\\ \cos\limits_{\wedge}{}_{T} &= Mean\left(\hat{T}_{GCIM}\right)\cdot\int\left(\hat{T}\cdot\cos\theta\right)dt\end{aligned}\right\} \quad (11)$$

$$\hat{T}_{Ampl} = 2\cdot\sqrt{\left(LPF\left(\sin\limits_{\wedge}{}_{T}\right)\right)^2+\left(LPF\left(\cos\limits_{\wedge}{}_{T}\right)\right)^2}, \quad (12)$$

$$sign = -\left(LPF\left(HPF\left(\hat{T}_{GCIM}\right)\cdot HPF\left(\hat{T}_{Aux}\right)\right)\right), \quad (13)$$

where: $\sin\limits_{\wedge}{}_{T}, \cos\limits_{\wedge}{}_{T}$ represent the sin and cos component of the estimated GCIM electromagnetic torque, θ represents the rotational angle, $\hat{T}_{GCIM}, \hat{T}_{Ampl}$ represent the GCIM electromagnetic torque and the amplitude of the estimated electromagnetic torque, $\hat{T}_{Aux}$ represents the estimated auxiliary motor electromagnetic torque, *sign* and offers information about the phase angle of the auxiliary motor torque and LPF, HPF are first-order low-pass and high-pass filters.

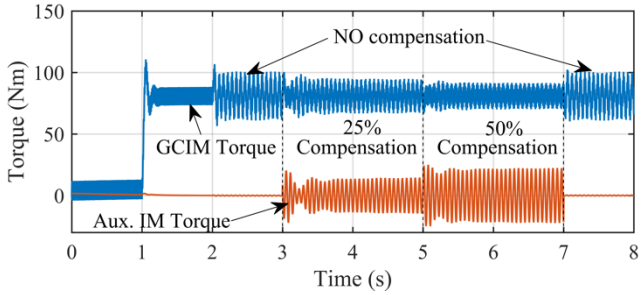

Fig. 14 – Closed-loop active torque pulsation damping – simulations.

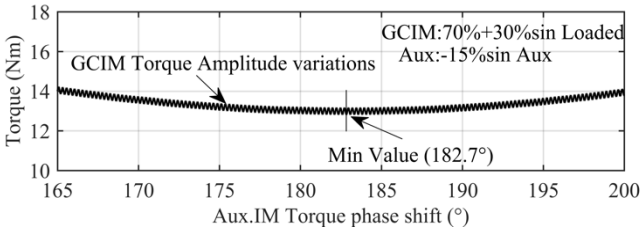

Fig. 15 – GCIM pulsation amplitude for variable compensating torque phase angle – simulation.

Figure 15 presents the GCIM electromagnetic torque amplitude variation for a given pulsating loading torque and a constant torque compensation in a variable phase shift. The maximum ATPRM efficiency (minimum GCIM torque amplitude) occurs at 182.7 deg. The 2.7 deg difference is probably due to the delay of the auxiliary motor variable frequency converter.

The profile of the load torque per revolution is constant in time. Both compensation levels (25 % and 50 %) refer to the amplitude of the pulsating torque. As the compensation reference increases, the PI controller modifies the reference to the auxiliary motor's VFC.

Besides the open-loop method, where the auxiliary VFC's compensating torque reference is given manually, the closed-loop method automatically changes the auxiliary IM electromagnetic torque amplitude (by VFC control) with the respective phase angle.

5. CONCLUSIONS

A new torque pulsation damping control technique was presented and validated in simulation and experiments.

An acceptable induction machine Luenberger-based inherently sensorless observer is given and used for online torque estimation.

It was proved that, in terms of grid-connected induction machine torque, a 46% pulsating torque compensation leads to a reduction of the fundamental pulsation amplitude by almost 65%., while a 60% compensation of the pulsating torque reduces the fundamental amplitude by nearly 84% (Fig. 11). In comparison, the torque 3rd-order harmonic does not show substantial changes with the torque compensation.

An acceptable criterion for the auxiliary machine (and VFC) power sizing can be established (according to fig. 7), where the absorbed grid power (GCIM+Aux. IM + VFC) is minimum.

Besides the principle of operation validation, the article introduces a new closed-loop torque pulsation damping mechanical parameter-free strategy which successfully reduces the GCIM torque pulsations to the desired value. As stated in Fig. 15, the compensation torque phase angle plays a key role in active torque pulsation damping strategy efficiency.

In the case of a load torque with a time-varying loading torque phase angle, more work related to real-time phase angle compensation is needed.

ACKNOWLEDGEMENT

The equipment and test benches required to fulfill this work were provided by Beespeed Automatizari SRL, Timisoara, Romania.

Received on 4 October 2022

REFERENCES

1. G. Zuo, L. Wong, *A review on recent active vibration control techniques*, arXiv, Jan. 22 (2016).
2. D. Miljković, *Review of active vibration control*, MIPRO Conference, Opatija, Croatia, pp. 103–108, (2009).
3. J. Liu, X. Zhang, C. Wang, R. Yan, *Active Vibration Control Technology in China*, IEEE Instrumentation & Measurement Magazine, **25**, *2*, pp. 36–44 (2022).
4. G. Reina, G.D. Rose, *Active vibration absorber for automotive suspensions: a theoretical study*, International Journal of Heavy Vehicle Systems, **23**, *1*, p. 21 (2016).
5. Q. Wang, K. Rajashekara, Y. Jia, J. Sun, *A Real-time vibration suppression strategy in electric vehicles*," IEEE Transactions on Vehicular Technology, **66**, *9*, pp. 7722–7729 (2017).
6. P. Gao, T. Yu, Y. Zhang, J. Wang, J. Zhai, *Vibration analysis and control technologies of hydraulic pipeline system in aircraft: a review*, Chinese Journal of Aeronautics, **34**, *4*, pp. 83–114 (2021).
7. R. Olaru, M.-M. Mihai, B. Gîrtan, C. Petrescu, A. Arcire, *Design and experiment of an electromagnetic vibrational inertial actuator using linearized magnetic spring*," Rev. Roum. Sci. Techn.– Électrotechn. et Énerg. **63**, *3*, pp. 253–258, Bucarest (2018).
8. T.-L. Le, T.-T. Huynh, C.-M. Lin, *Adaptive filter design for active noise cancellation using recurrent type-2 fuzzy brain emotional learning neural network*, Neural Comput & Applic, **32**, *12*, pp. 8725–8734 (2020).
9. J. Wang, J. Zhang, J. Xu, C. Zheng, X. Li, *An optimization framework for designing robust cascade biquad feedback controllers on active noise cancellation headphones,* Applied Acoustics, **179**, p. 108081 (2021).
10. T. Li et al., *Vehicle engine noise cancellation based on a multi-channel fractional-order active noise control algorithm*, Machines, **10**, *8*, Art. no. 8 (2022).
11. K. Nagata, H. Nemoto, T. Katayama, Y. Akita, *A sensorless control for damping of torsional vibrations with middle voltage induction motor*

drive for compressor application, Proc. of the 2011 14th European Conference on Power Electronics and Applications, Aug. 2011, pp. 1–10.
12. C. Ahumada, P. Wheeler, *Evaluation of input-shaping control robustness for the reduction of torsional vibrations*, IEEE Transactions on Industry Applications, **57**, *5*, pp. 5028–5038 (2021).
13. Q. Xu, W. Hong, "Dynamic performance of reciprocating compressor with capacity regulation system," *Proceedings of the Institution of Mechanical Engineers, Part E: Journal of Process Mechanical Engineering*, vol. 233, no. 3, pp. 526–535, Jun. 2019.
14. T. Feese, C. Hill, *Prevention of torsional vibration problems in reciprocating machinery*, Proceedings of the thirty-eighth turbomachinery symposium, pp. 213–238 (2009).
15. S.G. Chernyi, P. Erofeev, B. Novak, V. Emelianov, *Investigation of the mechanical and electromechanical starting characteristics of an asynchronous electric drive of a two-piston marine compressor*, Journal of Marine Science and Engineering, **9**, *2*, Art. no. 2 (2021).
16. C. Lascu, I. Boldea, F. Blaabjerg, *Comparative study of adaptive and inherently sensorless observers for variable-speed induction-motor drives*, IEEE Trans. on Industrial Electronics, 53, 1, pp. 57–65 (2006).
17. C. Lascu, I. Boldea, F. Blaabjerg, *A modified direct torque control for induction motor sensorless drive*, IEEE Transactions on Industry Applications, 36, 1, pp. 122–130 (2000).
18. A.D. Martin, L. Tutelea, R. Babau, I. Boldea, *A novel approach to PLCs based systems utilized in electric drives*, 2019 International Aegean Conference on Electrical Machines and Power Electronics (ACEMP) 2019 International Conference on Optimization of Electrical and Electronic Equipment (OPTIM), Aug. 2019, pp. 77–84.
19. A. Mechernene, M. Loucif, M. Zerikat, *Induction motor control based on a fuzzy sliding mode approach*, Rev. Roum. Sci. Techn.– Électrotechn. et Énerg., **64**, *1*, pp. 39–44, Bucarest (2019).
20. E G. Boudissa, F. Habbi, N.E.H. Gabour, M. Bounekhla, *A new dynamic genetic selection algorithm: application to induction machine identification*, Rev. Roum. Sci. Techn.– Électrotechn. et Énerg. Vol. 66, 3, pp. 145–151, Bucarest, 2021.
21. S. Medjmadj, D. Diallo, A. Arias, *Mechanical sensor fault-tolerant controller in pmsm drive: experimental evaluation of observers and signal injection for position estimation*, Rev. Roum. Sci. Techn.– Électrotechn. et Énerg., 66, 2, pp. 77–83 Bucarest (2021).